

Pyroelectrically induced photorefractive damage in magnesium-doped lithium niobate crystals

Judith R. Schwesyg,^{1,2,*} Matthias Falk,³ Chris R. Phillips,¹ Dieter H. Jundt,³
Karsten Buse,^{4,5} and Martin M. Fejer¹

¹*E. L. Ginzton Laboratory, Stanford University, Stanford, California 94305, USA*

²*Institute of Physics, University of Bonn, Wegelerstrasse 8, 53115 Bonn, Germany*

³*Crystal Technology, Inc., 1040 East Meadow Circle, Palo Alto, California 94303, USA*

⁴*Institute of Microsystem Technology, University of Freiburg, Georges-Köhler-Allee 102, 79110 Freiburg, Germany*

⁵*Fraunhofer Institute of Physical Measurement Techniques, Heidenhofstrasse 8, 79110 Freiburg, Germany*

*Corresponding author: schwesyg@physik.uni-bonn.de

Received February 18, 2011; revised May 24, 2011; accepted June 10, 2011;
posted June 27, 2011 (Doc. ID 142687); published July 21, 2011

Beam distortion due to photorefractive limits the usability of lithium niobate (LiNbO₃) crystals for frequency conversion applications. To prevent beam distortion in LiNbO₃, 5 mol.% magnesium-doped LiNbO₃ (MgO:LN) is usually used. However, we show that strong beam distortion of green laser light can occur within seconds in MgO:LN, starting at light intensity levels in the 100 mW/cm² regime, if the crystal is heated by several degrees Celsius during or before illumination. Beam distortion does not occur in undoped congruent LiNbO₃ (CLN) under the same conditions. We show that the pyroelectric effect together with an elevated photoconductivity compared to that of CLN causes this beam distortion and that this effect also influences frequency conversion experiments in the infrared even if no external heating is applied. © 2011 Optical Society of America

OCIS codes: 190.4400, 160.3730, 160.5320, 190.4870.

1. MOTIVATION

Efficient frequency conversion of laser light is of interest for numerous applications, especially for wavelengths where no cheap and efficient laser light sources are available, e.g., for green light or when broad wavelength tunability is desired. One of the most popular materials for nonlinear frequency conversion is lithium niobate (LiNbO₃), due to its high nonlinear optical coefficient [1] and low optical absorption over a wide wavelength range. With the development of quasi-phase-matching and its implementation in periodically poled LiNbO₃ [2] (and other ferroelectrics), practical application of frequency conversion became more widespread. Unfortunately, congruent LiNbO₃ (CLN) exhibits photorefractive damage (PRD), i.e., light-induced refractive index changes that alter the optical wavefronts and disturb the phase matching in nonlinear optical applications. PRD leads to beam distortion (often also called optical damage) and hence limits the maximum optical power that can be sent through a CLN crystal. Much effort has been put into solving this problem: There are several methods to reduce PRD, e.g., using thermoelectrically oxidized CLN [3] or heating the CLN crystal up to a temperature of about 200 °C [4]. However, the most common solution to this problem is to use magnesium-doped LiNbO₃ (MgO:LN) that contains at least 5 mol.% magnesium oxide (MgO) [5]. MgO:LN does not show PRD at even very high light intensities in the visible wavelength range [6,7]. The MgO doping changes some of the crystal properties significantly, e.g., the photoconductivity is 1–2 orders of magnitude larger in MgO:LN than in CLN (using green laser light), and the bulk-photovoltaic field is 2 orders of magnitude smaller in MgO:LN than in CLN [8]. These property changes are believed to inhibit PRD in MgO:LN; however, experiments in our labs indicated that

there are experimental circumstances when exactly these property changes can lead to PRD.

In an optical parametric oscillator (OPO) based on a periodically poled MgO:LN crystal that was pumped with 1064 nm laser light, we observed characteristic PRD in the uniformly poled parts of the crystal. The experiments indicated that the pyroelectric effect in combination with parasitic green light was related to this phenomenon.

This led us to the question if pyroelectrically induced PRD can be observed in MgO:LN, even though it is known to show no conventional bulk-photovoltaic PRD, by choosing a suitable light intensity and creating a pyroelectric field [9–12]. Another open question was why damage was not observed in CLN under similar conditions. In this paper we will first explore theoretically if pyroelectrically induced PRD is possible in MgO:LN. Therefore, we will examine the problem in one dimension and then extend the model to two dimensions in order to simulate more realistic experimental conditions. Second, we will also discuss the impact of our model on nonlinear optical applications, such as beam self-heating and inhibition of pyroelectrically induced PRD in MgO:LN. Finally, we will present experimental data in order to test our theoretical model.

2. INTRODUCTION

For nonlinear optical applications it is very important that the transmitted laser beam not be distorted or scattered. It is also crucial that there is no slowly varying refractive index change in the material along the propagation direction because this variation would decrease the conversion efficiency of nonlinear optical processes due to dephasing. Hence, optically

induced refractive index changes can be a serious obstacle in many applications.

A. Photorefractive Effect in Bulk-Photovoltaic Media

Optically induced refractive index changes are commonly referred to as photorefractive effects. In the case where this effect is unwanted, it is often referred to as PRD or optical damage, which can result from the combination of several effects.

Inhomogeneous illumination with light intensity $I(\mathbf{r})$ (\mathbf{r} is the spatial coordinate) causes a charge migration process due to drift, the bulk-photovoltaic effect, diffusion, or a combination of these effects. In a simplified picture, the bulk-photovoltaic effect can be described as a current taking the form $\mathbf{j}_{\text{phv}} = \beta I \hat{\mathbf{c}}$, where $\beta = \alpha_{33}$ is the bulk-photovoltaic constant of LiNbO₃ and α_{33} is the 33-component of the contracted third-rank bulk-photovoltaic tensor α_{ijk} [1] (note that implications of deviations from this simple model are discussed in Subsection 4.C.2) and $\hat{\mathbf{c}}$ is the crystal c axis; we furthermore assume $\hat{\mathbf{z}} \parallel \hat{\mathbf{c}}$ in the following sections. The drift current is given by $\mathbf{j}_{\text{drift}} = \sigma \mathbf{E}$, where σ is the conductivity and \mathbf{E} is the electric field. The diffusion current is given by $\mathbf{j}_{\text{diff}} = (k_b T/e) \mu_e \nabla \nu$ where k_b is the Boltzmann constant, T is the temperature, ν is the carrier density, and μ_e is the mobility. Note that the conductivity as well as the electronic mobility are in principle second-rank tensors, however in LiNbO₃ the tensor property can be neglected due to the isotropy of the conductivity and the electronic mobility tensors [13]. In contrast, in materials such as barium titanate (BaTiO₃) or Cr-doped strontium barium niobate mixed crystals [Cr:Sr_{0.61}Ba_{0.39}Nb₂O₆ (Cr:SBN)], electric tensor properties cannot be neglected [14,15]. Since we are focusing on LiNbO₃, we will neglect the tensor property of σ and μ_e . The charge transport can then be described by the total current density \mathbf{j} :

$$\mathbf{j} = \mathbf{j}_{\text{phv}} + \mathbf{j}_{\text{diff}} + \mathbf{j}_{\text{drift}} = \beta I \hat{\mathbf{z}} + (k_b T/e) \mu_e \nabla \nu + \sigma \mathbf{E}. \quad (1)$$

We assume intensities low enough that the photoconductivity is linear in the optical intensity, in which case the total conductivity is given by

$$\sigma = \kappa I + \sigma_d, \quad (2)$$

with κ being the specific photoconductivity and σ_d being the dark conductivity. Again, tensor properties of κ and σ_d can be neglected for LiNbO₃. The photoconductivity σ_{photo} can be described by $\sigma_{\text{photo}} = \kappa I$. Note that the electric field \mathbf{E} can also be determined by the electric potential ϕ through $\mathbf{E} = -\nabla \phi$. In this case Eq. (1) becomes

$$\mathbf{j} = -\sigma \nabla \phi + (k_b T/e) \mu_e \nabla \nu + \beta I \hat{\mathbf{z}}. \quad (3)$$

If a constant external potential difference is applied at the boundaries, e.g., the $+$ and $-z$ faces, ϕ splits up into an external and internal potential, i.e., $\phi = \phi_{\text{ext}} + \phi_{\text{int}}$. If the boundaries are far away from the beam and if the illuminated region is small compared to the dimensions of the crystal, the externally applied potential difference creates a constant electric field $\mathbf{E}_0 = -\nabla \phi_{\text{ext}}$. The total electric field can then be described as $\mathbf{E} = \mathbf{E}_0 - \nabla \phi_{\text{int}}$, and the boundary condition $\nabla \phi_{\text{int}} \rightarrow 0$ for $|\mathbf{r}| \gg w$, where w is the characteristic size of the beam such as the beam radius, has to be fulfilled.

The electro-optic effect creates a refractive index change according to

$$\Delta n_{o,e} = -n_{o,e}^3 r_{13,33} \frac{E_z}{2}, \quad (4)$$

with $n_{o,e}$ being the refractive indices for ordinarily and extraordinarily polarized light, respectively and $r_{13,33}$ being the elements of the electro-optic tensor (13 and 33 are contracted indices) with $r_{33} \approx 3r_{13}$ in LiNbO₃. The variable E_z is the z component of \mathbf{E} . In the following section we only consider extraordinarily polarized light; thus, $\Delta n = -n_e^2 r_{33} E_z / 2$ unless otherwise noted. If the electric field \mathbf{E} is inhomogeneous, as will be the case for any finite-diameter beam, the resulting refractive index distribution will be as well. This refractive index inhomogeneity leads to focusing or defocusing of the whole beam. It can also drive the evolution of smaller-scale index inhomogeneities that cause light scattering and characteristic dynamic light patterns in the far field [16]. These dynamic patterns together with the beam distortion are commonly referred to as PRD or optical damage. As mentioned in Section 1, PRD due to the bulk-photovoltaic effect is a serious problem for applications using CLN, but it is suppressed in MgO:LN crystals.

Note that, although the refractive index change is a whole-beam effect, the characteristic pattern formation, especially the dynamical substructures, might be caused on a microscopic scale. The exact mechanism by which these patterns build up is still under discussion. The theory most discussed in literature is photoinduced or so-called holographic light scattering; i.e., inhomogeneities such as the refractive index change cause weak initial scattering centers, which then act as seeds for subsequent holographic amplification [16,17]. However, it is beyond the scope of this article to go into detail concerning the dynamic substructure formation; here we focus on whole-beam effects, i.e., how the refractive index changes are caused on a macroscopic scale.

B. PRD Due to an Externally Applied Electric Field \mathbf{E}_0

It has been shown that PRD is caused not only by the bulk-photovoltaic effect but also by externally applied potential differences, i.e., external electric fields \mathbf{E}_0 , under simultaneous illumination; e.g., in LiNbO₃ doped with iron, bulk-photovoltaic photorefractive can be enhanced by application of an external electric field [18]. In the case where a homogeneous electric field \mathbf{E}_0 is applied to a non-bulk-photovoltaic (or only weakly bulk-photovoltaic) but photoconductive medium such as SBN, the refractive index is changed homogeneously according to Eq. (4) first, but as soon as the crystal is illuminated with, e.g., a Gaussian beam at a visible wavelength with \mathbf{E}_0 being present, the photoconductivity in the center of the beam becomes larger than in the outer wings of the beam or the dark parts of the crystal. Thus, the increased photoconductivity together with \mathbf{E}_0 causes a drift current that leads to screening of \mathbf{E}_0 in the center of the beam [9,19]. According to Eq. (4) this leads to a refractive index change within the beam profile, and, depending on the parameters of the beam, this can lead to beam distortion or even beam self-trapping. In the case of beam self-trapping, a so-called spatial bright screening soliton is formed [20].

C. Pyroelectrically Induced PRD

The pyroelectric effect in LiNbO_3 can generate an electric field, the so-called pyroelectric field \mathbf{E}_{pyro} , that influences photorefractive similarly to an externally applied electric field \mathbf{E}_0 . The pyroelectric effect is the change in spontaneous polarization \mathbf{P}_S of the crystal resulting from a change in temperature. In open-circuit condition a change in the spontaneous polarization results in a surface polarization charge, which, according to Gauss' law, generates an electric field \mathbf{E}_{pyro} . The pyroelectric coefficient $p_3 = dP_S/dT$ for LiNbO_3 is $-6.4 \times 10^{-5} \text{ CK}^{-1}\text{m}^{-2}$ [21]. The pyroelectric field in a z -cut plate, assuming homogeneous heating, is then given by

$$\mathbf{E}_{\text{pyro}} = -\frac{1}{\epsilon_{33}\epsilon_0} p_3 \Delta T \hat{z}, \quad (5)$$

where ϵ_0 is the permittivity of vacuum, ϵ_{33} is the tensor element of the static permittivity tensor $\hat{\epsilon}$, and ΔT is the temperature change. Equation (5) means that a temperature change of 1°C leads to $|\mathbf{E}_{\text{pyro}}| = 2.6 \text{ kV/cm}$. If the dark conductivity σ_d is small enough that the decay of the electric field is slow and if charge neutralization on the crystal surface is also weak, these fields can persist for several weeks [22]. Then, to a good approximation, \mathbf{E}_{pyro} can be treated as an external electric field \mathbf{E}_0 . That \mathbf{E}_{pyro} can substitute for \mathbf{E}_0 in photorefractive materials has already been shown by [11,12,23,24]; e.g., in [23] the authors show that they can create spatial screening-photovoltaic bright solitons [25] in CLN by applying pyroelectric fields instead of an external electric field. In [9,10] it has been shown that pyroelectric fields can cause beam distortion in materials such as barium strontium potassium sodium niobate (BSKNN), Ce-SBN:60, or SBN:60 that only show very weak or no bulk-photovoltaic effect [26]. For instance, in [9] a pyroelectric field was created by cooling a BSKNN, Ce-SBN:60, or SBN:60 crystal. Then the crystals were illuminated, and the observed phenomena were the same as if an external electric field would have been applied.

So far, PRD has not been reported to occur in MgO:LN with visible light. However, in the following sections we show theoretically and experimentally that pyroelectrically induced PRD exists. We also show that this effect does not occur in CLN under the same experimental condition it is predicted in MgO:LN .

3. THEORETICAL ANALYSIS OF PYROELECTRICALLY INDUCED PRD IN MgO:LN

In this section we present a theoretical model for pyroelectrically induced whole-beam refractive index changes in MgO:LN in order to derive the electric potential ϕ and electric field \mathbf{E} .

A. Steady-State Photorefractive Effect in the One-Dimensional Case

In order to determine whether the diffusion term is important or not, we first consider the steady-state case of Eq. (3) for the one-dimensional (1D) case with no external fields \mathbf{E}_0 applied and constant temperature. Note that 1D means that a uniformly poled crystal is considered and a planar beam propagates through the crystal along \hat{y} with the gradient of intensity parallel to \hat{z} .

In the following the crystal is illuminated with light of intensity $I(\mathbf{r}) = I_0 \bar{I}(\mathbf{r})$ with $\bar{I}(\mathbf{r}) \leq 1$. For a Gaussian intensity distribution in the planar case, the normalized intensity is $\bar{I} = \exp(-2\xi^2/w^2)$, where w is the characteristic beam size, e.g., the beam radius, and $\xi = z/w$ is the spatial coordinate normalized to w . We make the assumptions that local charge neutrality holds [27,28] and that the intensity is low enough that the conductivity is linear in intensity, i.e., $\sigma = \sigma_{\text{photo}} + \sigma_d = \kappa I + \sigma_d$. In order to simplify calculation, we introduce the so-called "equivalent dark intensity" I_d in analogy to [19,28], which is the intensity necessary to bring the photoconductivity up to the value of the dark conductivity. Then the conductivity can be written as $\sigma = \sigma_0 \bar{\sigma}(\mathbf{r}) = \sigma_0 [\bar{I}(\mathbf{r}) + \eta]$, where $\sigma_0 = \kappa I_0$ and $\eta = I_d/I_0$.

In steady state, the current from Eq. (1) must obey $\nabla \cdot \mathbf{j} = 0$; thus, the space-charge field generates a drift current $\mathbf{j}_{\text{drift}}$ balancing the other currents [28]. In the case of open-circuit boundary conditions, the total electric field is then obtained:

$$\mathbf{E}(\xi) = E_{\text{pv}} \frac{\bar{I}(\xi)}{\bar{I}(\xi) + \eta} \hat{z} + E_w \frac{d\bar{I}(\xi)/d\xi}{\bar{I}(\xi) + \eta} \hat{z}, \quad (6)$$

where the first term describes the bulk-photovoltaic field scaling with the characteristic bulk-photovoltaic field $E_{\text{pv}} = -\beta/\kappa$ and the second term describes the diffusion field E_{diff} with characteristic field $E_w = k_B T/(ew)$ [28].

B. Time Dependence of Pyroelectrically Induced PRD for the 1D Case

Assume that an unilluminated MgO:LN crystal of thickness H is uniformly heated to a temperature difference ΔT between the $+z$ and $-z$ faces. This temperature difference generates a pyroelectric field \mathbf{E}_{pyro} according to Eq. (5). Regarding \mathbf{E}_{pyro} as equivalent to an externally applied electric field [24], one can assume that there is a fixed voltage U applied across the crystal thickness H if the experiment is done within a time t smaller than the dark decay time. With this assumption it is possible to separate the bound charges (the pyroelectric charge) from the free charges originating from the photoconductivities and dark conductivities. If the crystal is then illuminated with an intensity $I(\mathbf{r})$ and we neglect the photovoltaic current and the diffusion, Eq. (1) simplifies to

$$\mathbf{j} = \sigma \mathbf{E}. \quad (7)$$

Note that, since we have formulated the transport as linear as discussed in Subsection 2.A, the pyroelectric field can be added to the bulk-photovoltaic field and the diffusion field given in Eq. (6). However, for cases of interest here, the pyroelectric field will be much larger than the bulk-photovoltaic field. Furthermore, since we are only considering whole-beam effects, the diffusion field is also orders of magnitude smaller than $|\mathbf{E}_{\text{pyro}}|$; e.g., for a $w = 100 \mu\text{m}$ and $T = 300 \text{ K}$, it is $E_w = 2.5 \text{ V/cm}$, while $|\mathbf{E}_{\text{pyro}}| = 2.6 \text{ kV/cm}$ for $\Delta T = 1^\circ\text{C}$. Thus, diffusion will be neglected in the further analysis as well.

The relation between the current \mathbf{j} and the space-charge density ρ is given by the continuity equation

$$\frac{\partial \rho}{\partial t} + \nabla \cdot \mathbf{j} = 0. \quad (8)$$

Then Eq. (8) together with Gauss' law and Eq. (7) yield

$$\nabla \cdot \left[\epsilon \epsilon_0 \frac{\partial \mathbf{E}}{\partial t} + \sigma \mathbf{E} \right] = 0 \quad (9)$$

with the solution

$$\epsilon \epsilon_0 \frac{\partial \mathbf{E}}{\partial t} + \sigma \mathbf{E} = \mathbf{j}_d, \quad (10)$$

where \mathbf{j}_d is a divergenceless current chosen to meet the boundary conditions.

Assume fixed-voltage boundary conditions, i.e., that there is a fixed voltage applied across the crystal thickness H . Then a current is flowing even in the absence of illumination, and in the case that the illuminated region is small in extent compared to the thickness H of the crystal, i.e., $w \ll H$, \mathbf{j}_d can be approximated by $\mathbf{j}_d = U \sigma_d \hat{\mathbf{z}}/H$. This simple model is appropriate for our pyroelectric case for times short compared to the dark decay time of the pyroelectric field. Using the notation from Subsection 3.A, the solution for Eq. (10) is then given by

$$\mathbf{E}(\bar{t}, \xi) = \frac{U}{H} \left\{ \frac{\eta}{\bar{I}(\xi) + \eta} + \frac{\bar{I}(\xi)}{\bar{I}(\xi) + \eta} \exp[-\bar{t}(\bar{I} + \eta)] \right\} \hat{\mathbf{z}}, \quad (11)$$

where $\bar{t} = t/\tau_{\text{di}}$ and $\tau_{\text{di}} = \epsilon \epsilon_0 / \sigma = \epsilon \epsilon_0 / [\sigma_0(\bar{I} + \eta)]$ with $\sigma_0 = \kappa I_0$. The time constant τ_{di} is also known as the characteristic Maxwell time, the characteristic time for buildup or decay of electric fields in the illuminated medium.

For $\bar{t} = 0$ it follows that $\mathbf{E} = (U/H)\hat{\mathbf{z}}$, which means that the field has not been screened in the illuminated region yet and is fully present. For the steady-state case $\bar{t} \gg 1$, one gets $\mathbf{E}(\bar{t}, \xi) = U\eta\hat{\mathbf{z}}/[H(\bar{I}(\xi) + \eta)]$, which is a nearly flat-top profile for the commonly encountered case of $\eta \ll 1$. Because of Eq. (4) the change in the electric field in the illuminated area of the crystal [Eq. (11)] leads to a refractive index change:

$$\Delta n = -\frac{1}{2} n_e^3 r_{33} \frac{U}{H} \left\{ \frac{\eta}{\bar{I}(\xi) + \eta} + \frac{\bar{I}(\xi)}{\bar{I}(\xi) + \eta} \exp[-\bar{t}(\bar{I} + \eta)] \right\}. \quad (12)$$

This refractive index change consists of two parts:

$$\Delta n = \Delta n_{\text{hom}} + \Delta n_{\text{ill}}. \quad (13)$$

First the homogeneous heating causes a homogeneous refractive index change

$$\Delta n_{\text{hom}} = -\frac{1}{2} n_e^3 r_{33} \frac{U}{H} \quad (14)$$

due to $\mathbf{E}_{\text{pyro}} = (U/H)\hat{\mathbf{z}}$. This homogenous refractive index change does not cause beam distortion. However, the subsequent illumination changes the refractive index inhomogeneously by

$$\Delta n_{\text{ill}} = -\frac{1}{2} n_e^3 r_{33} \frac{U}{H} \left(\frac{\bar{I}(\xi)}{\bar{I}(\xi) + \eta} \left\{ \exp[-\bar{t}(\bar{I} + \eta)] - 1 \right\} \right). \quad (15)$$

Note Δn_{ill} and Δn_{hom} have opposite signs. The refractive index change Δn_{ill} normalized to $-\Delta n_{\text{hom}}$ is shown in Fig. 1.

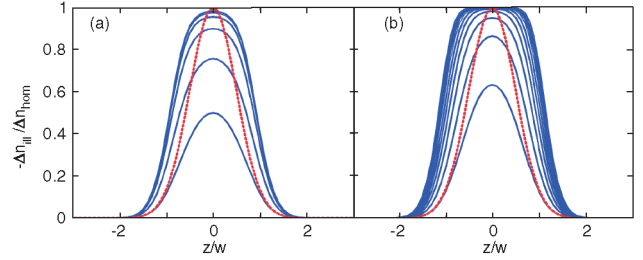


Fig. 1. (Color online) Pyroelectrically induced refractive index change Δn_{ill} (normalized to $-\Delta n_{\text{hom}}$) versus $\xi = z/w$. (a) refractive index change plotted for $t = 5\tau_{\text{di}}$ and $\eta = 0.1^l$ with $l = 0, 0.5, 1, 1.5, \dots, 4$ (from smallest to largest refractive index change). The curves for $l = 2, \dots, 4$ overlap each other. (b) refractive index change plotted for $t = 0, 1, \dots, 10 \times \tau_{\text{di}}$, and $\eta = 0.001$ (from inside to outside). In both graphs \bar{t} is shown as red dashed line.

In Fig. 1(a) the normalized refractive index change is plotted for $t = 5\tau_{\text{di}}$ and varying η . In Fig. 1(b) the normalized refractive index change is plotted for varying time t and $\eta = 0.001$. In both graphs \bar{t} is shown as a red dashed line. Note that, for $\eta \rightarrow 1$, screening cannot be reached. This is the case when $\sigma_d = \sigma_0$.

The phenomenological explanation is the same as in Subsection 2.B; due to the increased photoconductivity in the center of the illuminated part of the crystal, E_{pyro} can be screened faster there than in the wings of the Gaussian light intensity distribution where the lower photoconductivity leads to slower screening of E_{pyro} . In the dark part of the crystal the entire pyroelectric field persists. This change in the electric field leads to a refractive index change according to Eq. (4), as can be seen in Fig. 1. Especially for times where the flat part of the refractive index profile has not yet developed, the transmitted beam will be distorted and partially deflected due to the refractive index change in the illuminated region. However, one can also expect that beam distortion will be reversed once the flat-top profile has developed because the beam would not be disturbed anymore.

C. Finite-Difference Time-Domain Simulations for the Two-Dimensional Case

In order to solve the problem in the two-dimensional (2D) case, the corresponding general equations must be derived. The 2D steady-state solution has already been derived by [19], the time-dependent equations have been solved numerically for the model system bismuth titanate $\text{Bi}_{12}\text{TiO}_{20}$ with an external electric field applied, which neglects a bulk-photovoltaic current and diffusion [29]. Similar simulations can also be applied for the case of MgO:LN as is shown in the following. Again we assume that a MgO:LN crystal is heated uniformly first, generating an electric field $\mathbf{E}_0 = \mathbf{E}_{\text{pyro}}$, and that \mathbf{E}_{pyro} is constant within the time frame of the experiment. The diffusion term is neglected as in Subsection 3.B since we are only considering whole-beam effects. After \mathbf{E}_{pyro} has been established, illumination with a laser beam with Gaussian intensity distribution is switched on. In the following we focus on the time dependence of the charge distribution ρ of free charge carriers, which is determined by the continuity equation [Eq. (8)]. Substituting Eq. (3) into Eq. (8) one obtains

$$\frac{\partial \rho}{\partial t} = -\{\kappa(\mathbf{E}_0 - \hat{\mathbf{z}}E_{\text{pv}}) \cdot \nabla I - \nabla \cdot [(\kappa I + \sigma_d)\nabla \phi_{\text{int}}]\}. \quad (16)$$

Furthermore, the Poisson equation gives the relation between ϕ_{int} and ρ :

$$-\frac{\rho}{\epsilon_0} = \epsilon_{11}\partial_x^2\phi_{\text{int}} + \epsilon_{11}\partial_y^2\phi_{\text{int}} + \epsilon_{33}\partial_z^2\phi_{\text{int}}. \quad (17)$$

Unfortunately, there is no analytical solution to this problem; however, it can be solved numerically with finite-difference time-domain (FDTD) calculations that give a solution for ρ and ϕ . Then it is possible to determine the total electric field \mathbf{E} .

We performed FDTD simulation for the 2D case based on Eqs. (16) and (17). For the calculation, a Gaussian light intensity distribution was assumed, and $|E_{\text{pv}}| \ll |E_{\text{pyro}}|$.

Concerning σ_d , there hardly exist any data for CLN and MgO:LN for $T < 100^\circ\text{C}$ because CLN and MgO:LN crystals are quite good electrical insulators for temperatures below 150°C . In CLN one can assume that σ_d is in the range 10^{-16} – $10^{-18}(\Omega\text{cm})^{-1}$ [22]. For as-grown MgO:LN crystals doped with 5 mol.% MgO, an upper bound for σ_d at room temperature has been determined $\sigma_d \leq 2 \times 10^{-15}(\Omega\text{cm})^{-1}$ [30]. In another publication σ_d of MgO:LN doped with 5 mol.% MgO was of the order of $10^{-16}(\Omega\text{cm})^{-1}$ [31] at room temperature. From [8,31] it then becomes clear that σ_d in MgO:LN is at least 2 to 3 orders of magnitude smaller than $\sigma_0 = \kappa I_0$ in the intensity range 1–10 W/cm². Therefore, we neglect σ_d in Eqs. (16) and (18) for all cases where I_0 is of the order of 1 W/cm² or higher. This approximation will not affect the refractive index changes significantly in the region $|r|/w < 2$ for MgO:LN. Furthermore, one can expect that σ_0 and σ_d are not affected by small temperature changes of less than 10°C .

Figure 2 shows the time dependence of the refractive index change Δn_{ill} . Since $\hat{\epsilon}$ represents a tensor, a characteristic dielectric time constant has to be defined, which approximately describes an exponential time dependence of the z component of the space-charge field for $t \approx 0$ in the center of the illuminated region. For LiNbO₃ and the z component of the electric field, it is given by [32]

$$\tau_{\text{di}} = \frac{\epsilon_0(\epsilon_{33} + \sqrt{\epsilon_{33}\epsilon_{11}})}{\kappa I + \sigma_d}. \quad (18)$$

Hence, time t in Fig. 2 was normalized to τ_{di} . The refractive index change Δn_{ill} was normalized to Δn_{hom} . The 2D simulations show the screening of the pyroelectric field in the areas of increased σ_{photo} . With increasing time, similar to the 1D case, a flat-top refractive index profile develops in the illuminated area. In the dark areas of the crystal, the entire

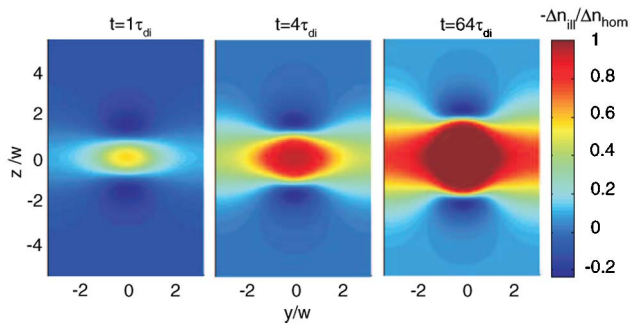


Fig. 2. (Color online) Numerically simulated normalized refractive index change $-\Delta n_{\text{ill}}/\Delta n_{\text{hom}}$. The ratio of $\epsilon_{11}/\epsilon_{33}$ is 2.9, as is the case for MgO:LN.

pyroelectric field is present, and the refractive index is unchanged. However, the 2D case is also a bit different from the 1D case. Similar to conventional PRD in CLN, the characteristic side lobes in the $+z$ and $-z$ directions develop with an opposite sign with respect to that of the flat area in the middle [19]. Figure 3 depicts z cuts through the refractive index profile beam center $\Delta n_{\text{ill}}(y=0, z)$ normalized to $-\Delta n_{\text{hom}}$ for different illumination times t in multiples of τ_{di} . Again similarities to the 1D case are obvious.

Note, the 2D simulations are suitable to the extent that no beam distortions occur. In order to take into account beam distortions and scattering effects, three-dimensional (3D) simulations have to be performed, which will be described elsewhere.

D. Impact on Applications Due to Pyroelectrically Induced PRD in MgO:LN

One simple solution to inhibit pyroelectrically induced PRD due to homogeneous heating simply is to short circuit the c faces of the crystal, e.g., by applying a conductive paste on the c faces and electrically connecting them with each other. This connection prevents the crystal from accumulating surface charges during heating or cooling; hence, pyroelectric fields cannot develop. However, if a nonlinear optical device with a periodically poled MgO:LN (PPMgOLN) crystal is pumped by a strong infrared pump beam, spatially inhomogeneous self-heating occurs, and thus local temperature increase can induce local pyroelectric fields that cannot be fully screened by short circuiting the surfaces of the crystal. That pyroelectric effects due to beam self-heating with visible laser light can occur in pyroelectric media has been reported from experimental observation in SBN [33]. There, the pyroelectric fields lead to lensing. The same can be expected to happen in MgO:LN if just a strong enough infrared pump beam is used because there is always residual optical absorption inside the crystal. Since, at the same time, high average power infrared lasers usually generate some parasitic visible light in PPMgOLN due to accidentally phase-matched frequency conversion processes [34], this parasitic light would then partially screen the pyroelectric fields, and hence a very inhomogeneous pyroelectrically induced refractive index profile would be the consequence.

In the following sections, a new theoretical model for the pyroelectrically induced PRD in MgO:LN due to beam

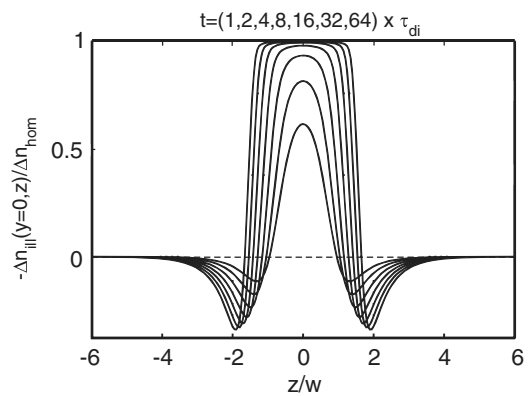


Fig. 3. Numerically simulated refractive index change $\Delta n_{\text{ill}}(y=0, z)$ in MgO:LN for varying illumination times $t = 1\tau_{\text{di}}, 2\tau_{\text{di}}, 4\tau_{\text{di}}, 8\tau_{\text{di}}, 16\tau_{\text{di}}, 32\tau_{\text{di}}, 64\tau_{\text{di}}$ (smallest to largest Δn_{ill}).

self-heating will be developed, and a method to reduce this effect will be presented.

1. Beam Self-Heating in a Uniformly Poled MgO:LN Crystal

In the case of a uniformly poled MgO:LN crystal in which a laser beam is partially absorbed, there will be a radially varying temperature rise in addition to an increase in the average temperature of the crystal. The pyroelectric effects associated with the average temperature rise can be eliminated by shorting the z faces of the crystal, as discussed in Subsection 3.D. However, the spatially varying part of the temperature will create a volume polarization charge, which cannot be screened by the surface but will be screened by the volume conductivity of the crystal. Thus, in the case of beam self-heating, we also have to include the heat equation into our model. As already mentioned, pyroelectrically induced lensing was reported experimentally in SBN [33]; here we analytically and numerically investigate this effect and its implications for MgO:LN.

In the case of self-heating, it is possible to get analytic solutions for the space-charge fields involved in the pyroelectrically induced PRD only for times short compared to the dielectric relaxation time. We will derive some approximations for the temperature and pyroelectric field before we solve the problem with FDTD simulations.

First, we determine the temperature field. The heat equation is given by

$$\left(\frac{1}{k_{\text{th}}}\frac{\partial}{\partial t} - \nabla^2\right)\Delta T = \frac{q(\mathbf{r})}{\lambda_{\text{th}}}, \quad (19)$$

where ΔT is the temperature rise above the original temperature, q is the heat generated per unit volume per unit time by absorption of the optical beam, k_{th} is the thermal diffusivity, and λ_{th} is the thermal conductivity. Furthermore, it is $k_{\text{th}} = \lambda_{\text{th}}/\rho c_p$, where ρ the mass density and c_p is the heat capacity. Note that k_{th} and λ_{th} are second-rank tensors. The anisotropy of these properties can again be neglected for LiNbO₃ [35]; in other media they may have to be taken into account. For an intensity distribution $I(\mathbf{r})$ and absorption coefficient α , the heat source term q is given by

$$q(\mathbf{r}) = \alpha I(\mathbf{r}) = \alpha I_0 \bar{I}(\mathbf{r}), \quad (20)$$

where we normalize the intensity to its peak value, I_0 .

From Eq. (19), the thermal field in the steady state obeys

$$\nabla^2(\Delta T) = -q(\mathbf{r})/\lambda_{\text{th}}. \quad (21)$$

It is convenient to normalize the temperature according to $\Delta T(\mathbf{r}) = T_0 \Delta \bar{T}(\bar{\mathbf{r}})$, where $T_0 = \alpha I_0 w^2/\lambda_{\text{th}}$ is the temperature field amplitude and $\bar{\mathbf{r}} = \mathbf{r}/w$ (in the 1D case it is $\xi = z/w$). In terms of optical power $P = \pi I_0 w^2/2$, for a Gaussian beam it is

$$T_0 = 2P\alpha/(\pi\lambda_{\text{th}}). \quad (22)$$

With these definitions Eq. (21) can be written

$$\bar{\nabla}^2(\Delta \bar{T})(\bar{\mathbf{r}}) = -\bar{I}(\bar{\mathbf{r}}). \quad (23)$$

The solution $\Delta T(r)$ of Eq. (21) for a Gaussian beam $I(r) = I_0 \exp[-2(r/w)^2]$ at radius r from the heat source in a cylindrical sample with radius R is given in terms of exponential integral functions [36]:

$$\Delta T(r) = \frac{\alpha P}{4\pi\lambda_{\text{th}}} \left[-E_i\left(-2\frac{R^2}{w^2}\right) + E_i\left(-\frac{2r^2}{w^2}\right) - 2\ln\left(\frac{r}{R}\right) \right]. \quad (24)$$

The boundary condition at $r = R$ is taken to be $\Delta T(r = R) = 0$. The on-axis asymptotic form ($\mathbf{r} \rightarrow 0$) of Eq. (24) is

$$\Delta T(0) \approx \frac{\alpha P}{4\pi\lambda_{\text{th}}} \left[\gamma_{\text{Euler}} + \ln\left(2\frac{R^2}{w^2}\right) \right], \quad (25)$$

where $\gamma_{\text{Euler}} \sim 0.577215\dots$ is Euler's constant. In the next step we estimate the maximum pyroelectric field that can build up due to beam self-heating. The appropriate analysis of this situation will depend on the time constants for the thermal field to become established versus τ_{di} . The time for the portion of the thermal field varying across the beam region to become established is of the order of the thermal diffusion time $\tau_{\text{th}} = w^2/(4k_{\text{th}})$. For $w = 50 \mu\text{m}$, $\lambda_{\text{th}} \approx 5 \text{ W}/(\text{m K})$, $\rho \approx 4.64 \text{ g}/\text{cm}^3$, and $c_p \approx 0.5 \text{ J}/(\text{g K})$ [35], as would be appropriate for a confocally focused beam of $1 \mu\text{m}$ radiation in a 20 mm long LiNbO₃ crystal, the thermal diffusion time is $\tau_{\text{th}} \approx 0.001 \text{ s}$. In contrast, τ_{di} can be months in CLN in the dark or several weeks in MgO:LN. Under illumination with green light of intensity $100 \text{ W}/\text{cm}^2$, the time constant τ_{di} in CLN can be several minutes [37] and of the order of seconds in MgO:LN [8]. Hence, we assume that the steady-state thermal field is established before the polarization charge is significantly screened. It should be borne in mind that, for sufficiently large samples, non-negligible screening could occur before the thermal field has diffused to the edges of the crystal.

From [32] it can be derived that the z component of the pyroelectric field in the beam center, before charge screening starts, takes the form

$$E_{z,\text{pyro}} \approx -\frac{p_3 T}{\epsilon_0 (\epsilon_{33} + \sqrt{\epsilon_{33}\epsilon_{11}})} \quad \text{for } t \ll \tau_{\text{di}}, \quad (26)$$

where the anisotropy factor $\epsilon_{33} + \sqrt{\epsilon_{33}\epsilon_{11}}$ for the z component of the pyroelectric field in the beam center is used according to [32]. Thus, a characteristic pyroelectric field is defined for the beam self-heating case by substituting Eq. (25) into Eq. (26):

$$E_{\text{pyro}} \approx -\frac{p_3 \alpha P \left[\gamma_{\text{Euler}} + \ln\left(\frac{2R^2}{w^2}\right) \right]}{4\pi\lambda_{\text{th}}\epsilon_0 (\epsilon_{33} + \sqrt{\epsilon_{33}\epsilon_{11}})}. \quad (27)$$

For 2D temperature diffusion in the slablike crystal geometry used in practice, the temperature rise of the beam center also depends logarithmically on the size of the crystal. We find that, for an estimate for the temperature rise of the beam center, in this case $\ln(2R^2/w^2)$ can be replaced with $\ln[0.5(\min[L_y, L_z]/w)^2]$, where L_y and L_z are the dimensions of the crystal in the y or z direction, respectively. Note that the scaling of E_{pyro} in the beam self-heating case is qualitatively different between the 1D and 2D geometries. This

difference arises because the temperature rise at the beam center is much smaller when thermal diffusion occurs in two dimensions rather than one.

In order to determine the electric field for all \mathbf{r} and times t in the case of beam self-heating, 2D FDTD simulation was performed by taking Eq. (21) into account in addition to Eq. (16) and (17). Again it was assumed that $\sigma_{\text{photo}} = \kappa I$. The potential ϕ and the charge distribution ρ were determined for a slab-shaped crystal, but by taking into account that the total time-dependent charge density is a sum of pyroelectric and free electronic charge densities ($\rho = \rho_{\text{pyro}} + \rho_{\text{free}}$) with

$$\rho_{\text{pyro}}(\mathbf{r})(\mathbf{r}, t = 0) = -\nabla \cdot (\Delta \mathbf{P}_s) = -\nabla \cdot (p_3 \Delta T(\mathbf{r})\hat{z}), \quad (28)$$

where \mathbf{P}_s is the spontaneous polarization. Again we used $\sigma \approx \kappa I$ and $t_{\text{th}} = w^2/(4k_{\text{th}}) = 0.001$ s. As boundary conditions $\phi = 0$ and $\Delta T = 0$ have to be fulfilled at the crystal surfaces at all times, we assume that the crystal surface is perfectly heat sunk to a fixed temperature and electrically grounded. The conductivity is again $\sigma = \kappa I + \sigma_d$ where σ_d was neglected.

As a result the cut $E_z(y = 0, z, t)$ through the electric field profile along the z axis is shown in Fig. 4 for different times (multiples of τ_{di}). For $t = 0$ the curve is parabolic around $y = z = 0$, while for longer times a flat-top profile starts to develop. For convenience the plot is normalized to E_{pyro} [Eq. (27)]. Thus, for short times the pyroelectric field causes an imperfect lensing effect, but for intermediate times a rather hard edge in the pyroelectric field (and therefore in the refractive index profile) develops in the region of significant intensity, which can cause PRD. Whole-beam diffractive and holographic effects can be calculated in 3D by adding the x axis as the light-propagation direction into the simulations and including beam diffraction to calculate the resulting electric field $\mathbf{E}_{\text{optical}}(x, y, z, t)$, but this is beyond the scope of this article.

As a practical example, according to Eq. (22) a LiNbO₃ crystal with an absorption coefficient $\alpha = 0.005 \text{ cm}^{-1}$ illuminated with a Gaussian beam of power $P = 20$ W would change the steady-state temperature difference across the beam by about 1.2 K and create a pyroelectrically induced refractive index change before screening (extraordinarily polarized) of the order of -2×10^{-5} . In comparison, a temperature change of 1.2 K would create a thermo-optic refractive index change

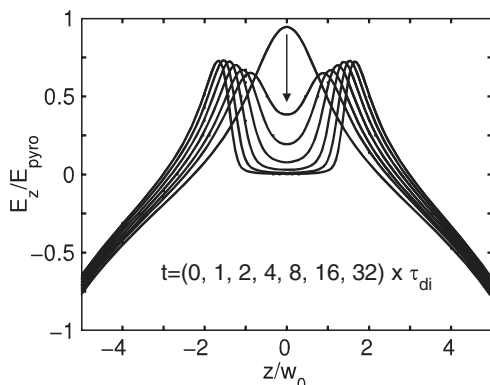


Fig. 4. Cut $E_z(y = 0, z, t)$ through the 2D electric field profile along the z axis for the beam self-heated case for different times (multiples of τ_{di}) and slablike crystal shape. For $t = 0$ the curve is parabolic around $y = z = 0$; for longer times a flat-top profile starts to develop. The electric field is normalized to E_{pyro} from Eq. (27).

of 4×10^{-5} (thermo-optic coefficient of LiNbO₃ $dn_e/dT|_E = 3.3 \times 10^{-5} \text{ K}^{-1}$ [35]). Considering a typical beam radius of, e.g., $w = 100 \mu\text{m}$, and a crystal length of $L = 20$ mm, such a thermo-optic lens would have a focal length

$$f \approx \frac{\pi w^2 \lambda_{\text{th}}}{\alpha P L (dn/dT)} \quad (29)$$

of about 20 mm [38]. The pyroelectrically induced refractive index change before charge screening starts creates a defocusing lens where the focal length is of the same order of magnitude as the thermo-optic lens. But due to charge screening, the pyroelectrically induced refractive index change will become spatially even more inhomogeneous (Fig. 4) for times exceeding the dielectric relaxation time. Hence, thermo-optic and pyroelectric refractive index changes will not cancel out each other but will lead to a very inhomogeneous refractive index profile, which will cause beam distortion and light scattering. This combined lensing effect illustrates the importance of pyroelectrically induced refractive index changes. We consider means for mitigating beam self-heating effects after discussing the impact of periodic poling on the magnitude of the pyroelectrically induced index changes.

2. Electric Fields Due to Beam Self-Heating in a Periodically Poled MgO:LN Crystal

Although homogenous pyroelectric fields can be short circuited in principle, in the case of beam self-heating, short circuiting the z facets will not completely solve the problem (Fig. 4). One solution might be homogeneous illumination of the crystal with UV light as was shown in [39]. However, there might be an even easier solution to the problem: periodic poling. It was already theoretically shown that the bulk-photovoltaic PRD is strongly suppressed in periodically poled CLN [28]. In the following we will show that a similar analysis can be applied to the pyroelectrically induced PRD.

Consider the same basic assumptions as in case of beam self-heating in a uniformly poled crystal, but include a domain pattern varying periodically along y with a fundamental spatial frequency $K_g = 2\pi/\Lambda$ (Λ is the poling period), so that, noting that the pyroelectric coefficient varies from positive to negative sign in oppositely oriented domains, it can be written as

$$p(y)/p_3 = a_0 + \sum_{m=1}^{\infty} a_m \cos(mK_g y + \nu_m), \quad (30)$$

where $a_0 = 2D - 1$, $a_m = 4 \sin(\pi m D)/(\pi m)$, with D being the quasi-phase-matching (QPM) duty cycle, and p_3 is again the bulk pyroelectric coefficient. The DC term a_0 is proportional to the deviation in the duty cycle from its ideal value (for odd-order QPM) of 50%. For $D = 50\%$ and for a grating whose first domain is centered at $y = 0$, it is $a_0 = 0$, $a_m = 4/(m\pi)$ for $m = 1, 5, 9, \dots$, $a_m = -4/(m\pi)$ for $m = 3, 7, 11, \dots$, $a_m = 0$ for m even, and the $\nu_m = 0$.

According to Eq. (28) and a vector identity, it can be shown that the pyroelectric charge density ρ_{pyro} is $\rho_{\text{pyro}}(\mathbf{r}, t = 0) = -\hat{z} \cdot \nabla [p(y)\Delta T(\mathbf{r})]$. For short times $t \ll \tau_{\text{di}}$, the pyroelectric field obeys $\nabla \cdot \mathbf{E} = \rho_{\text{pyro}}/\epsilon\epsilon_0$. The problem is most conveniently solved in terms of the potential rather than directly for E_{pyro} [28]:

$$\nabla^2 \phi = \frac{\hat{\mathbf{z}} \cdot \nabla [p(y) \Delta T(\mathbf{r})]}{\epsilon \epsilon_0}, \quad (31)$$

where the potential can be taken in the form

$$\phi(\mathbf{r}) = \Phi_0(x, z) + \sum_{m=1}^{\infty} \Phi_m(x, z) \cos(mK_g y + \nu_m). \quad (32)$$

Since we only consider the case where $\hat{\mathbf{c}} \parallel \hat{\mathbf{z}}$, it follows

$$\nabla^2 \phi = \frac{p(y)}{\epsilon \epsilon_0} \hat{\mathbf{z}} \cdot \nabla [\Delta T(\mathbf{r})]. \quad (33)$$

For simplicity we discuss the planar case where $I = I(z) = I_0 \bar{I}(z)$, $\xi = z/w$, and $\Delta T(z) = T_0 \Delta \bar{T}(\xi)$. With Eqs. (30), (32), and (33) and projecting out the various coefficients, the m th term in Eq. (31) obeys

$$(\nabla_t^2 - m^2 K_g^2) \Phi_m(x, z) = \frac{p_3 a_m}{\epsilon \epsilon_0} \hat{\mathbf{z}} \cdot \nabla_t [\Delta T(\mathbf{r})], \quad (34)$$

where $m = 0, 1, 2, \dots, \infty$ includes the DC term as well as those with spatial modulation and $\nabla_t = \nabla - \mathbf{y} \partial / \partial y$. Equation (34) then becomes

$$\left(\frac{d^2}{d\xi^2} - m^2 K_g^2 w^2 \right) \Phi_m(\xi) = \frac{p_3 T_0 a_m}{\epsilon \epsilon_0} w \frac{d\Delta \bar{T}(\xi)}{d\xi}. \quad (35)$$

In the case of uniform poling, i.e., $m = 0$, and with $\mathbf{E} = -\hat{\mathbf{z}} d\phi/dz$, one obtains $E(z) = -p_3 a_0 \Delta T(z) \hat{\mathbf{z}} / (\epsilon \epsilon_0)$, which is consistent with E_{pyro} in Eq. (5). As mentioned in [28], $K_g^2 w^2$ is usually quite large, e.g., for $\Lambda = 30 \mu\text{m}$ and $w = 50 \mu\text{m}$, which are typical numbers for a PPMgOLN crystal used for OPOs, $K_g^2 w^2 = 110$. Thus, in the case $m^2 K_g^2 w^2 \gg 1$, Eq. (35) becomes simply

$$\Phi_m(\xi) = -\frac{p_3 T_0 a_m}{\epsilon \epsilon_0} \frac{1}{m^2 K_g^2 w^2} \frac{d\Delta \bar{T}(\xi)}{d\xi}. \quad (36)$$

With Eq. (23), $T_0 = \alpha I_0 w^2 / \lambda_{\text{th}}$, and in analogy to Eq. (32) $E_z(y, z) = E_{z,0}(z) + \sum_{m=1}^{\infty} E_{z,m}(z) \cos(mK_g y + \nu_m)$, the transverse component of the electric field is

$$E_{z,m}(z) = -\frac{1}{w} \frac{\partial \Phi_m(y, \xi)}{\partial \xi} = -\frac{p_3 \alpha I_0 w^2 a_m}{\epsilon \epsilon_0 \lambda_{\text{th}}} \frac{1}{m^2 K_g^2 w^2} \bar{I}(\xi). \quad (37)$$

There also is a longitudinal field $E_y(y, z)$ that can be derived similarly, but in analogy to the photovoltaic case discussed in [28] it is not important for this analysis because it is $\pi/2$ out of phase with the domain grating and hence does not significantly contribute to the average electro-optic refractive index change.

In order to determine the electro-optic refractive index change according to Eq. (4), the same analysis as in [28] is done by expanding the electro-optic tensor r/r_{33}^{eff} in a Fourier series like $p(y)/p_3$ in Eq. (30). Then the refractive index change is

$$\Delta n_{e, \text{PPMgOLN}} = -\frac{p_3 T_0}{\epsilon \epsilon_0} \frac{n_e^3 r_{33}^{\text{eff}}}{2} \left[a_0 + \sum_{m=1}^{m=\infty} \frac{a_m}{2} \cos(mK_g y + \nu_m) \right] \times \left[E_{z,0} + \sum_{m=1}^{m=\infty} E_{z,m} \cos(mK_g y + \nu_m) \right]. \quad (38)$$

Because of the fact that, for $D \sim 50\%$, $a_1 \gg a_0$ and $a_m \propto 1/m$ in Eq. (38), terms for $m > 1$ and mixed terms can be neglected in the Fourier series. Thus, a good approximation is

$$\Delta n_{e, \text{PPMgOLN}} \approx -\frac{p_3 T_0}{\epsilon \epsilon_0} \frac{n_e^3 r_{33}^{\text{eff}}}{2} \left[a_0^2 \Delta \bar{T}(\xi) + \frac{a_1^2}{2K_g^2 w^2} \cos^2(K_g y) \bar{I}(\xi) \right]. \quad (39)$$

The refractive index change in a uniformly poled crystal due to beam self-heating is [Eq. (26)] $\Delta n_{e,u} = -p_3 T_0 n_e^3 r_{33}^{\text{eff}} / (2\epsilon \epsilon_0)$; thus, in a PPMgOLN crystal with 50% duty cycle, it is

$$\frac{\Delta n_{e, \text{PPMgOLN}}}{\Delta n_{e,u}} \approx \frac{8}{\pi^2} \frac{1}{(K_g w)^2} \frac{\bar{I}(\xi)}{\Delta \bar{T}(\xi)}. \quad (40)$$

Equation (40) shows that the electro-optic index change in PPMgOLN is suppressed by a factor $(\pi K_g w)^2 / 8$ compared to that in uniformly poled MgO:LN, which is $1/140$ for $\Lambda = 30 \mu\text{m}$ and $w = 50 \mu\text{m}$. It also shows that the refractive index perturbation is proportional to the intensity profile $\bar{I}(\xi)$ in PPMgOLN, whereas it is proportional to the temperature change profile $\Delta \bar{T}(\xi)$ in the case of uniform poling. Note that, for PPMgOLN, in the 2D case $\Delta n_{e, \text{PPMgOLN}} \propto d^2(\Delta T) / d\xi^2$.

The previous analysis was made under the assumption of a perfect 50% QPM duty cycle. However, if there is a duty cycle error of $a_0 = 2D - 1$, suppression is less effective and the DC term ($m = 0$) in Eq. (39) adds a significant contribution when

$$a_0^2 = (2D - 1)^2 > \frac{8}{\pi^2} \frac{1}{(K_g w)^2}, \quad (41)$$

e.g., for $\Lambda = 30 \mu\text{m}$ and $w = 50 \mu\text{m}$ and $D \approx 54\%$, the maximum refractive index suppression is $\Delta n_{e, \text{PPMgOLN}} / \Delta n_{e,u} \approx 1/70$, which is already only half of that for $D = 50\%$. With a deviation from a perfect duty cycle, pyroelectric fields can build up due to beam self-heating and therefore can lead to pyroelectrically induced PRD. The above analysis shows that, even if there is only a small portion of the light path where there are duty cycle errors or where periodic poling is totally missing, e.g., at the crystal edges, PRD can occur, especially in resonators. If that is the case, it is very likely that using a strong infrared pump beam that generates parasitic green or blue light, whose photogenerated carriers partially screen the pyroelectric fields, can cause pyroelectrically induced PRD in the PPMgO:LN sample in addition to conventional thermo-optic lensing effects.

The theoretical analyses in Subsections 3.B–3.D are not limited to MgO:LN in principle but could apply to other periodically poled photoconductive ferroelectrics as well.

4. EXPERIMENTAL SETUPS AND RESULTS

In the previous sections we have developed a model for pyroelectrically induced whole-beam photorefractive effects in

MgO:LN. In the following sections we present experimental data.

The experiments were performed with several 5 mol.% MgO:LN and undoped CLN crystals provided by Crystal Technology, Inc. For comparison and in order to make sure that the results are not crystal-grower specific, MgO:LN crystals from Yamaju Ceramics Co., Ltd., were also used. All crystals were polished to high optical quality on the x facets of the crystals. Table 1 summarizes all samples used in the experiments.

A. Beam Distortion

1. Setup and Experimental Procedure

Prior to each measurement, the crystal under investigation was thoroughly cleaned with acetone, water, and methanol. Then the crystal was placed on a heated aluminum block, which itself was mounted on a three-axis translation stage. Before the start of any experiment, the crystal was thermally equilibrated to the initial oven temperature T_i , and electric charge that may have been generated pyroelectrically or deposited on the crystal surfaces during handling was removed by short circuiting the z faces of the crystals temporarily. Then the crystal was put in open-circuit condition again.

The crystal was illuminated with a Gaussian beam of 532 nm radiation from a frequency-doubled continuous-wave Nd:YAG laser, linearly polarized along the crystallographic z axis and propagating along the x direction of the crystal. The temperature of the crystal was controlled with a temperature accuracy of $\pm 0.1^\circ\text{C}$ at the surface of the crystal in contact with the heating block; the temperature was also measured at the opposite (air) surface of the crystal. During illumination, the crystal was heated until the top and bottom of the crystal reached stable T_f . Experiments were also carried out with the illumination applied after the crystal had been thermally equilibrated at the final temperature T_f .

The setup is shown schematically in Fig. 5. Before the beam entered the crystal, it passed through a half-wave plate and a polarizer, which, together with neutral density filters, enabled continuous adjustment of the power P incident on the crystal from $20\ \mu\text{W}$ to 2 W. The beam was focused at the center of the crystal to a $1/e^2$ intensity diameter $2w$, which was $100\ \mu\text{m}$ in all experiments unless otherwise noted. The incident beam was extraordinarily polarized, i.e., polarized along the z axis of the crystal. The transmitted beam was observed on a screen placed approximately 50 cm beyond the output face of the crystal. Various temperature differences $T_f - T_i$ were applied in several experiments; however, T_f was always kept below 50°C . After illumination was stopped, the c faces of the crystal were short circuited to discharge any pyroelectric surface charges, and the crystal was cooled down to T_i . Note that

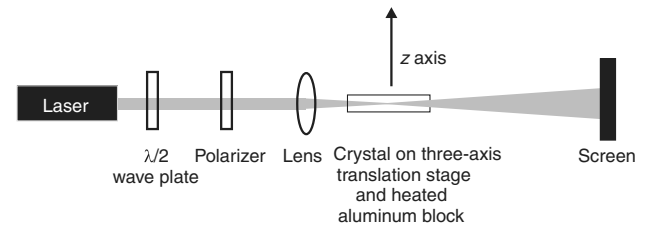


Fig. 5. Setup for the observation of beam distortion. The laser is a 532 nm frequency-doubled continuous-wave Nd:YAG laser.

any internal space-charge fields that may have been created during illumination would not be erased by this process [9].

2. Results

Before investigating the effects of changing the temperature of the MgO:LN crystals, we first carried out measurements on samples CTIMgOLN₁, CTIMgOLN₂, and YamMgOLN₁ at constant temperature to examine their conventional photovoltaic PRD behavior. For these measurements, the crystals were illuminated along the x axis, first with $P = 2\ \text{W}$ and then with $P = 20\ \mu\text{W}$. No measurable PRD was observed in any of the MgO:LN crystals (less than 1% change in diameter on the screen in the far field).

To investigate the effects of varying temperature, the MgO:LN samples were then illuminated at a constant power of $20\ \mu\text{W}$, and the temperature was ramped from $T_i = 40^\circ\text{C}$ to $T_f = 50^\circ\text{C}$. A picture of the beam shape transmitted through sample YamMgOLN₁ at different stages of the experiment is shown in Fig. 6. All MgO:LN samples showed similar behavior. Less than 1 s after initiation of the temperature ramp, PRD could be observed with typical beam distortion and far-field pattern formation. After several seconds, the original beam shape could not be recognized anymore [Fig. 6(b)]; however, the beam shape continued to evolve. Beam distortion remained even after the crystal equilibrated to T_f . Finally, after a several minutes in this stage the beam shape began to restore slowly toward its original shape, but it did not fully recover. Scattered light could still be observed in the region outside the original beam diameter even after 1 h elapsed [Fig. 6(c)].

In another experiment the samples were heated first and then, after thermal equilibration at T_f , were subject to subsequent illumination with the same beam parameters as described above in order to create optical damage. Illumination is started once the selected temperature has been reached. Note that, between heating and illumination, the crystal c facets were not short circuited again. In all the samples the beam showed similar distortion as seen in Fig. 6(b).

To investigate the persistence of these photorefractive effects, MgO:LN crystals with PRD were stored at room temperature in the dark for times up to several weeks and then

Table 1. Crystals Used in the Experiments and Their Short Names

Crystal Type	Dimensions	Short Name
	$x\ \text{mm} \times y\ \text{mm} \times z\ \text{mm}$	
CLN	$20 \times 20 \times 20$	CLN ₁
CLN	$9 \times 11 \times 1$	CLN ₂
Crystal Technology MgO:LN	$9 \times 11 \times 1$	CTIMgOLN ₁
Crystal Technology MgO:LN	$9 \times 11 \times 0.5$	CTIMgOLN ₂
Crystal Technology MgO:LN	$25 \times 25 \times 25$	CTIMgOLN ₃
Crystal Technology MgO:LN	$25 \times 15 \times 20$	CTIMgOLN ₄
Yamaju MgO:LN	$10 \times 12 \times 0.5$	YamMgOLN ₁

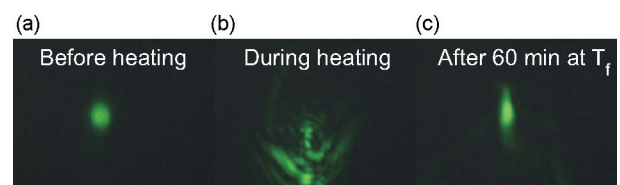


Fig. 6. (Color online) Shape of a laser beam after passing an MgO:LiNbO₃ crystal (sample YamMgOLN₁) that is heated from 40°C to 50°C . (The c axis is parallel to the vertical dimension in the photographs).

probed optically with the same 532 nm beam as was used in the previous experiments. Scanning the beam along the y axis of the crystal on a path that intersected the previously damaged spot resulted in scattered light when the beam intersected the regions displaced slightly to the $+y$ and $-y$ side of the previously illuminated and damaged spot. In contrast, in areas where no PRD had been created earlier, no PRD was observed. For this experiment the crystal was not heated in order to make sure that the transmitted beam could not create any additional optical damage.

It was also shown that the PRD could be completely erased by homogeneously illuminating the crystal with an incandescent lamp for 30 min. After that exposure the beam diameter in the far field was within 1% of its original value. For applications, it is important to note that, after erasing the optical damage with white light, the MgO:LN crystals could be used for subsequent experiments without any apparent change in properties.

Similar experiments were also conducted with different starting temperatures and temperature differences; however, T_f was never higher than 50 °C. All experiments revealed the same qualitative behavior. However, when the incident power was increased to $P = 100$ mW rather than the $P = 20$ μ W used in the previous experiments, the strong distortion shown in Fig. 6(b) was not observed but the weak scattering in the wings of the beam [as in Fig. 6(c)] was still observed. The effect again persisted for weeks in crystals stored in the dark.

It is very important to note that the beam was not distorted and no patterning occurred in any experiment when the z faces of the MgO:LN crystal were short circuited during heating, e.g., by painting silver conducting paste on the z faces and connecting them with each other. Furthermore, conducting the experiment with sample CLN₂, PRD could not be observed with 20 μ W optical power and 100 μ m beam diameter, whether or not a temperature step was applied during illumination. However, at higher laser powers (of the order of milliwatts) at room temperature, the conventional bulk-photovoltaic PRD [16] could be observed in CLN independent of heating, whereas, as already noted, bulk-photovoltaic PRD was not observed in MgO:LN under these conditions.

B. Interferometry

1. Setup

A Zygo laser interferometer and Zygo MetroPro data processing software were used to image any whole-beam refractive index changes inside the crystals associated with the above observed optical damage to compare with predictions from Subsection 3.C. Crystals were first exposed to 532 nm radiation and temperature changes as described in Subsection 4.A. However, since the spatial resolution of the Zygo interferometer is about 100 μ m, it was necessary to generate a refractive index distribution of significantly greater spatial extent to have a reasonable number of pixels in the interferogram, which was accomplished by using a collimated 532 nm beam of 5 mm diameter rather than the 100 μ m beam used in the previous experiments. Hence, the illumination setup depicted in Fig. 5 was adjusted: a second lens was placed into the beam behind the first lens in order to have a collimated beam with diameter $d = 5$ mm. Thus, only the large crystals CTIMgOLN₃, CTIMgOLN₄, and CLN₁ could be used in this experiment. However, the heating-and-illumination part of the experiment was

performed in the same way as described in Subsection 4.A. Note that the temperature at the top of the large crystals was generally 0.4 °C lower than that at the bottom of the crystal, but as the diameter of the optical beam was small compared to the crystal dimension, the effective pyroelectric field in the area where the beam illuminated the crystal could be seen as constant and, indeed, within the accuracy of measurement, so no effect of the temperature gradient was measured. In the following we took the temperature measured at the bottom in order to determine ΔT in our experiments. In order to have reproducible conditions, the sample with initial temperature $T_i = 23$ °C was equilibrated to temperature $T_i + \Delta T = T_f$ with no illumination (over approximately 15 min), after which illumination was initiated. Subsequent to illumination, the crystal was short circuited while cooling down to room temperature after which it was characterized with the Zygo interferometer. Note that, in different experiments, different illumination times were used; the longest illumination times used was 160 s.

The Zygo interferometer used light at $\lambda = 632.8$ nm with an intensity that was orders of magnitude smaller than the intensity of the green writing beam. The sample was placed in the interferometer with the x axis almost parallel to the measurement beam; a slight tilt of the crystal inhibited multiple back-reflections into the detector. The Zygo MetroPro software was able to correct for that tilt later. The interferometer measured variations in the optical path length $OPL = \int_C n(s) ds$, where C is the geometrical path and s is the distance along the path C . Hence, the optical path difference (OPD) did not only depend on the change in the refractive index but also on the change in geometrical path. However, the Zygo MetroPro software was able to correct for OPDs caused by crystal thickness variations due to, e.g., curved or tilted surfaces. In addition, as a cross check, we also took measurements of the unprocessed crystals in order to measure OPD due to thickness variations, surfaces roughness, or refractive index inhomogeneities that were present before the experiment was performed. Thus, the interferometric data were corrected for these variations.

2. Results

Interferometric measurements with unprocessed as-grown MgO:LN samples showed that the crystal length L was constant between subsequent measurements to an accuracy of about half a wavelength; thus, any larger OPD (compared to the unprocessed crystal) after heating, illumination, and short circuiting could be attributed to refractive index changes Δn_{ill} , which could be determined as deviations from uniformity from the corrected OPD data. Note that the measurement procedure did not allow the determination of absolute numbers for the refractive index; it could only determine refractive index deviations from uniformity.

Some typical results of the Zygo interferometer measurements after heating and subsequent illumination of a MgO:LN crystal are shown in Fig. 7 for different illumination times. For these measurements, sample CTIMgOLN₄ was used with $\Delta T = 2$ °C and $P = 150$ mW. Depicted are the OPDs within the crystal normalized to $2L$, i.e., the distance the light travels within the crystal in the interferometric setup. The results shown in Fig. 7 were corrected for tilt and misalignment of the sample within the interferometer arm by using the Zygo MetroPro software. They were not corrected for crystal thickness variations,

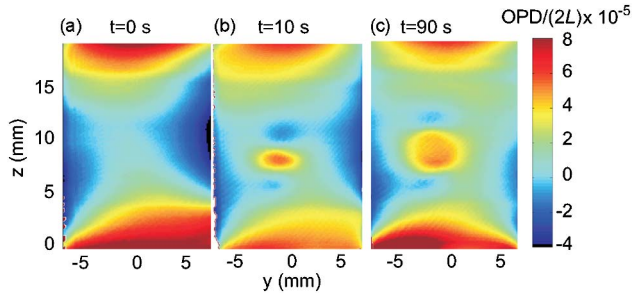


Fig. 7. (Color online) OPD map of CTIMgOLN₄ for $\Delta T = 2^\circ\text{C}$ and $P = 150\text{ mW}$: (a) unprocessed, (b) after 10 s, and (c) after 90 s of illumination. Data are normalized to $2L$.

surface roughness errors, or as-grown refractive index inhomogeneities yet in order to show the significance and character of the effect. Prior to heating and illumination, the crystal was examined with the Zygo interferometer in order to obtain the OPD map [Fig. 7(a)] of the as-grown crystal. Then the sample was illuminated for 10 s using the experimental routine described in Subsection 4.B without heating. No change in optical path length could be observed with respect to Fig. 7(a). This shows that illumination itself did not cause thickness or refractive index variations. After that the experiment was repeated with heating and subsequent illumination for 10 s [Fig. 7(b)]. An optical path length change in the area where the crystal was illuminated can be clearly seen. After this measurement, the pattern was erased by illuminating the sample with white light homogeneously for 30 min. No OPD with respect to Fig. 7(a) could be measured after white light illumination. Then the heating-and-illumination experiment was repeated; in this case the illumination time was 90 s [Fig. 7(c)]. It is important to note that it is not possible to place the crystal exactly in the same position in the illumination setup and the Zygo interferometer in every measurement. Therefore, Fig. 7 shows slightly different crystal positions. From Fig. 7(a) it becomes obvious that the crystal surfaces are curved; this effect can also be seen in Figs. 7(b) and 7(c). However, even though the surfaces are curved, one can clearly see that, after 10 s of illumination, the optical path length is changed positively in the beam center. After 90 s of illumination, a shape similar to a flat-top profile develops. One can also see that the change in optical path length cannot be attributed to a change in crystal thickness since it is an order of magnitude larger than the crystal thickness change measured before. The observed OPD in the illuminated area can only be attributed to refractive index changes Δn_{ill} [according to Eq. (13)]; thickness variations, e.g., due to temperature variations or the converse piezoelectric effect, can be excluded. Another remarkable feature is that a local negative refractive index change seems to develop in a lobelike shape in regions below and above the region of positive refractive index change in the center of Figs. 7(b) and 7(c).

In another experiment the crystal was slightly cooled. Although the temperature excursion in this case could not be evaluated quantitatively, a refractive index measurement could be performed after illumination, using the same beam parameters as in Fig. 7. The refractive index profile looked very similar to Figs. 7(b) and 7(c), but, in this case, the refractive index change in the beam center was negative, and the side lobes were positive.

In order to quantify the z dependence of the nonuniform refractive index change Δn_{ill} going through the beam center,

the experiment was repeated varying the illumination times and intensities for sample CTIMgOLN₄. The same experimental routine of heating and illumination was used again with $\Delta T = 3^\circ\text{C}$ and $P = 150\text{ mW}$. Maps of OPD as in Fig. 7 were obtained and not only corrected for tilts but also for surface curvature of the crystal, surface roughness, etc. Thus, we could determine $\Delta n_{\text{ill}}(y = 0, z, t)$, which is depicted in Fig. 8. The accuracy of the measured refractive index changes is estimated to be about 20%, due to a number of parameters that were not well controlled. In particular, although the crystal z surfaces were electrically insulated from each other, screening of the pyroelectric field by external charges could not be inhibited; e.g., it was not possible to control how well the surface was cleaned; it was also not possible to control the humidity and other environmental factors that could lead to surface charge screening. Furthermore, temperature gradients were probably present near the crystal surfaces, and their influence on the pyroelectric field could not be controlled. Another error source was the Zygo interferometer, which suffered from room temperature fluctuations that could easily be detected.

Figure 8 shows that, with increasing illumination time, a positive flat-top refractive index profile develops with negative side lobes in $+z$ and $-z$ directions. It also shows that there is a maximum refractive index change in the beam center. In Fig. 9, the normalized refractive index change in the beam center $\Delta n_{\text{ill}}(y = 0, z = 0, t)$ from Fig. 8 is plotted versus illumination time t (squares). The solid line represents the result of the FDTD simulations from Subsection 3.C for $\tau_{\text{di}} = 14\text{ s}$. Note that, in contrast to the case of 1D illumination (Subsection 3.B), the time dependence of the refractive index change is not an exponential function, as was also seen to be the case for 2D bulk-photovoltaic PRD in CLN [32].

In Fig. 10 the refractive index change $\Delta n_{\text{ill}}(y = 0, z, t = 20\text{ s})$ is shown for different intensities but fixed illumination time $t = 20\text{ s}$. The developing flat-top refractive index profile can be seen again as well as the negative refractive index side lobes.

The above experiments were also performed with sample CTIMgOLN₃, and the same qualitative behavior was seen as was depicted in Figs. 7, 8, and 10 for sample CTIMgOLN₄. In contrast, in CLN₁ no refractive index change profile was measured with the Zygo interferometer within the refractive

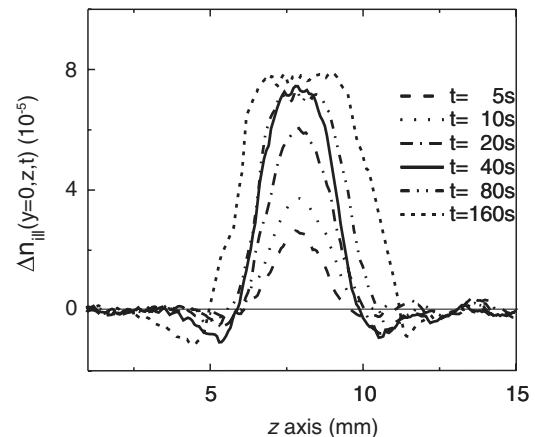


Fig. 8. Nonuniform refractive index change $\Delta n_{\text{ill}}(y = 0, z, t)$ in CTIMgOLN₄ for different illumination times $t = 5, 10, 20, 40, 80, 160\text{ s}$. Experimental parameters were $\Delta T = 3^\circ\text{C}$ and $P = 150\text{ mW}$.

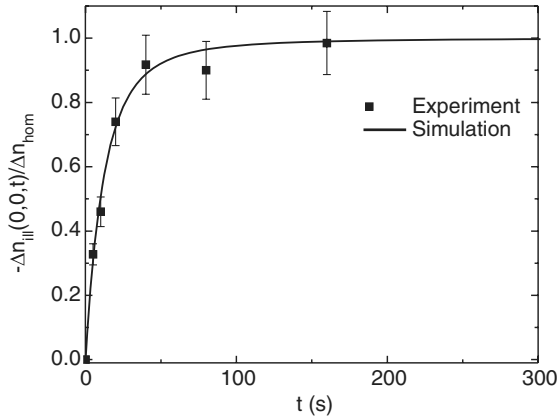


Fig. 9. Normalized maximum refractive index change $\Delta n_{||l}(y=0, z=0, t)$ versus illumination time t (squares) in sample CTiMgOLN₄. The solid line represents the result of the numerical simulation for $\tau_{di} = 14$ s.

index change accuracy of about 2×10^{-6} and a maximum illumination time of 160 s. This also is consistent with the observation that, in CLN, no beam distortion could be observed after heating and illumination with low light intensity.

C. Determination of κ and β

In the previous theoretical description it has been pointed out that knowledge of β , σ_{photo} (or the specific photoconductivity κ), and σ_d are crucial for the understanding of the pyroelectrically induced PRD. Experimental data about σ_{photo} and β in CLN and MgO:LN already exist [8]; however, crystals grown ten years or more ago had different impurity levels than the ones grown recently, and quantities like κ strongly depend on impurity levels. In a more recent study [37], σ_{photo} and β were measured over a wide intensity range for CLN but not for MgO:LN crystals. Hence, it is necessary to measure these quantities on crystals that have been grown under the same conditions as the crystals used in the PRD experiments described in Subsection 4.B.2. By determining κ and σ_d , one can calculate τ_{di} [Eq. (18)] and compare it to the τ_{di} determined in Fig. 9.

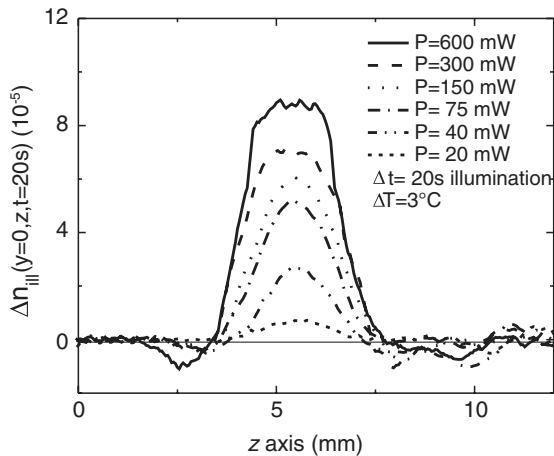


Fig. 10. $\Delta n_{||l}(y=0, z, t=20$ s) of sample CTiMgOLN₄ for different laser powers $P = 600, 300, 150, 75, 40, 20$ mW (largest to smallest refractive index change). Experimental parameters were $\Delta T = 3^\circ\text{C}$ and the illumination time $t = 20$ s.

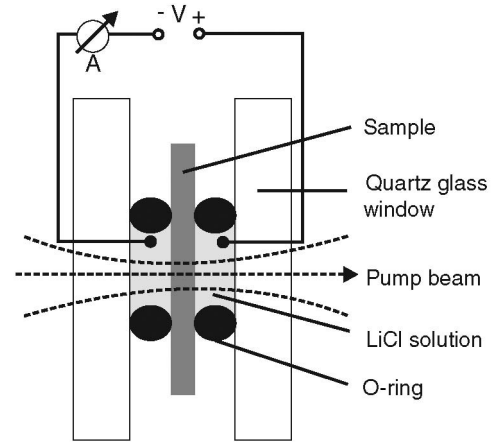


Fig. 11. Schematic of the apparatus for measurement of photoconductivity and bulk-photovoltaic current.

1. Setup

For these measurements we used an electric-field-poling cell depicted in Fig. 11 [40]. This apparatus was chosen to allow electrical contacting of the surfaces without significant absorption of the incident laser power in the electrical contacts, thereby minimizing heating and the interference from the concomitant pyroelectric currents. Typical photocurrents in these samples are of the order of picoamperes, so care must be taken to minimize these and other interfering currents. In this setup the crystal sample (typical dimension $10\text{ mm} \times 10\text{ mm} \times 1\text{ mm}$) was clamped with two silicone rubber o-rings between two quartz-glass plates. An electrolyte, saturated lithium chloride (LiCl) solution, was filled between the gaps inside the o-rings. The two LiCl-filled chambers were electrically connected with platinum wires to a Keithley 618 programmable picoammeter, which measured the electrical current flowing through the sample in the z direction and which could also apply a voltage in order to measure conductivity. The 514 nm wavelength output of an argon-ion laser was focused through the quartz-glass windows, the electrolyte, and the sample. Since no 532 nm source was available for these measurements, we chose the 514 nm Ar-laser line. This wavelength was chosen to be the strongest Ar-ion laser line that is closest to $\lambda = 532$ nm, which was the writing wavelength in the experiments described in Subsection 4.B.2. The light intensity was varied over the range 10^1 – 10^4 W/cm² by translating the focusing lens on a translation stage; thus, only intensity changed but not the power of the laser beam. With this arrangement the heat input due to residual absorption in the crystal is constant, minimizing pyroelectric current artifacts associated with absorption-induced temperature changes in the crystal. The following currents were measured.

- Bulk-photovoltaic current I_{pv} : laser on, voltage off.
- Dark current I_d : laser off, voltage on, i.e., 10 V for MgO:LN and 80 V for CLN samples.
- Total current I_{tot} : laser on and voltage on, 10 V for MgO:LN and 80 V for CLN samples.

Then the photoconductive current I_{photo} , the specific photoconductivity κ , and the bulk-photovoltaic coefficient β were determined according to

$$\bullet I_{photo} = I_{tot} - I_d - I_{pv}.$$

- $\kappa = I_{\text{photo}}/(E \cdot P)$, with E being the applied electric field.
- $\beta = I_{\text{pv}}/P$.

2. Results

The specific photoconductivity κ of samples CLN₂ and CTIMgOLN₁ are shown in Fig. 12. It was not possible to measure κ and β for samples CTIMgOLN₄, CTIMgOLN₃, and CLN₁ directly because of their crystal dimensions. However, note that sample CTIMgOLN₁ was produced under comparable crystal growth conditions as CTIMgOLN₄ and CTIMgOLN₃, and sample CLN₂ was comparable to CLN₁. By repeating the measurements, the error for κ turned out to be about $\pm 20\%$ (repeated measurements) because the measurements were extremely sensitive to various parameters, e.g., vibrations, temperature changes, and leakage currents. Figure 12 clearly shows that κ is about 30 times smaller in CLN than in MgO:LN. In both cases κ varies by less than a factor of ≈ 3 over an intensity range of 3 orders of magnitude.

It was not possible to determine σ_d . The minimum resolvable current in our apparatus, 10 fA, exceeded the dark currents in both CLN and MgOLN, so it was not possible to measure the dark conductivities with the maximum bias voltages available. The upper limit for σ_d in our measurements was $\sigma_d \leq 5 \times 10^{-16} (\Omega \text{ cm})^{-1}$. This observation is consistent with other determinations of σ_d for the dark conductivities for MgO:LN [30].

The photocurrents at light intensities in the range $I = 0.1\text{--}10 \text{ W/cm}^2$ were smaller than our resolution limit of 10 fA for the beam diameters available here, so we have assumed from the near constancy of the results for κ over the measured range of $10^1\text{--}10^4 \text{ W/cm}^2$ that the same values are applicable at lower intensities. The specific photoconductivity κ of MgO:LN and CLN was also determined for many other MgO:LN and CLN samples that are not listed here and that came from various vendors and different crystal growth runs. It turned out that the values for κ for various MgO:LN crystals (5 mol.% MgO doped) vary between 0.1 and 0.5 pS cm/W. For CLN crystals κ values were in the range of 0.001–0.008 pS cm/W.

The intensity dependence of the bulk-photovoltaic coefficient β is depicted in Fig. 13. The error for β was about $\pm 10\%$ (repeated measurements). Figure 13 shows that β is 1 order of magnitude smaller in MgO:LN than in CLN at high intensities but nearly equal at lower intensities. It is also re-

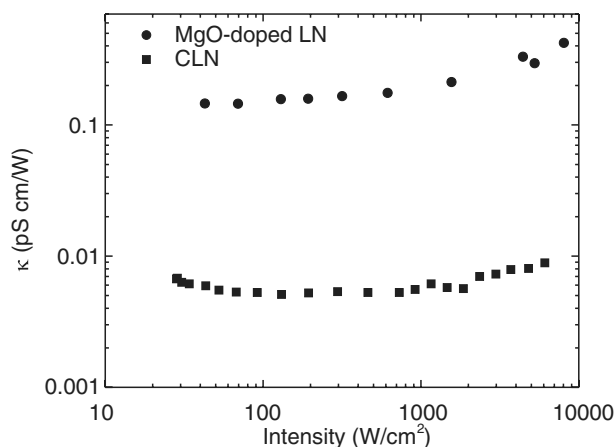


Fig. 12. Specific photoconductivity versus intensity for CLN (squares) and MgO:LN (circles).

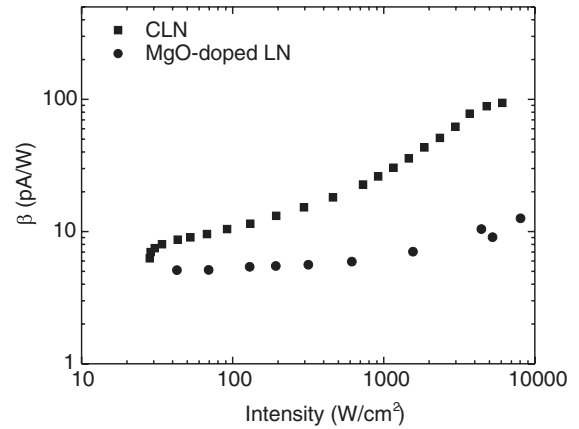


Fig. 13. Bulk-photovoltaic coefficient β versus intensity for CLN (squares) and MgO:LN (circles).

markable that β is sublinear ($\beta \propto I^{0.5}$) in intensity for CLN and rather constant for MgO:LN ($\beta \propto I$), as we assumed in Subsection 2.A. That β is sublinear over a wide intensity range is in agreement with [37].

As already mentioned, we were not able to make reliable photocurrent measurements in the intensity range $I = 0.1\text{--}10 \text{ W/cm}^2$, but also in this case one can assume that the value for β at $I = 0.1\text{--}10 \text{ W/cm}^2$ was similar to the closest β data point in Fig. 13.

5. DISCUSSION

The experimental results clearly showed that pyroelectrically induced PRD exists in MgO:LN. We conclude that the observed PRD in Subsections 4.A and 4.B were induced by the pyroelectric effect because the refractive index changed only when the sample was heated and when the sample z facets were electrically insulated from each other. It was also shown that the sign of the refractive index change depends on the sign of the temperature change. In contrast, the sign and magnitude of the changes in the refractive index due to the bulk-photovoltaic effect do not depend on small temperature changes.

The experimental results shown in Figs. 7 and 8 agree well with the FDTD simulations in Fig. 2 and in Fig. 3 within measurement accuracy. Even the side lobes can be identified both in simulations and experimental results. Simulations and experimental results also agree for the time dependence of the refractive index change shown in Fig. 9. The theoretical curve with $\tau_{\text{di}} = 14 \text{ s}$ fits the data very well. And as a cross check according to Eq. (18), this value of τ_{di} corresponds to a specific photoconductivity $\kappa = 0.27 \text{ pS cm/W}$, which agrees with obtained data in Fig. 12.

Figure 10 shows why it seems as if at higher optical intensities there is no PRD. Indeed there is a refractive index change; the higher intensity just leads to a faster buildup of the flat-top profile so that PRD seems not to occur at high laser powers. So far it was widely assumed that suppression of PRD in MgO:LN also means that there are not any light-induced refractive index changes. Our measurements show that this assumption no longer holds. Even if a laser beam is not distorted, writing long-lasting refractive index channels into MgO:LN can be an obstacle for nonlinear optical applications because as soon as the beam shape is slightly

changed, e.g., due to a setup change, these changes can at least temporarily limit the performance of the device.

The expected theoretical maximum refractive index change of $\Delta n_{\text{ill}}(y=0, z=0)_{\text{max}} = -\Delta n_{\text{hom}} = 1.3 \times 10^{-4}$ for $\Delta T = 3^\circ\text{C}$ [Eq. (14)] was similar to the experimentally observed $\Delta n_{\text{ill}}(y=0, z=0)_{\text{max}} = 0.8 \times 10^{-4}$; the origin of the discrepancy of a factor 1.5 is not clear. Since $\Delta n_{\text{hom}} \propto E_{\text{pyro}}$, this result indicates that the actual $|E_{\text{pyro}}|$ is smaller than expected. This observation is a common issue with pyroelectric fields since external charge screening and other effects can lower the measured $|E_{\text{pyro}}|$ [9,24]. It also has to be taken into account that, in our apparatus, the top always was a bit cooler than the bottom of the crystal; hence, the actual ΔT in the area of the beam might be lower than the temperature change measured at the bottom. For the 0.4°C temperature difference discussed in Subsection 4.B, this effect would induce a difference in the refractive index change between top and bottom by about 2×10^{-5} . Thus, this could at least partly explain the discrepancy in the refractive index changes. Although $|E_{\text{pyro}}|$ is smaller than expected, effects such as partial surface screening or temperature errors do not affect the time dependence, which was consistent with time constants calculated from transport measurements described in Subsection 4.C.2.

The refractive index inhomogeneity due to heating and illumination of MgO:LN crystals is correlated with the beam distortions in Fig. 6(b). Similar to conventional bulk-photovoltaic PRD, it appears that the refractive index inhomogeneity in the illuminated area acted as an initial light scatterer that seeds subsequent holographic amplification [17], which in turn leads to the diffuse and distorted beam shapes shown in Fig. 6(b). Quantitative analysis of the dynamics of this process remains a topic for future research. After the flat-top refractive index profile develops, the refractive index inhomogeneity is located in the wings of the beam, reducing the seed power available for the holographic amplification so that the far-field scattering is reduced and the beam shape is restored.

Note that pyroelectrically induced PRD did not occur in our experiments with CLN crystals under the same experimental conditions. In fact our experiments and simulations show that the behavior of MgO:LN is more similar to that of a medium having no bulk-photovoltaic effect, such as SBN [9], than to CLN which has a strong bulk-photovoltaic effect. From Figs. 12 and 13 the differences in transport properties between CLN and MgO:LN becomes clear. From the measured values of β and κ in Subsection 4.C.2 the bulk-photovoltaic field E_{pv} can be calculated according to $E_{\text{pv}} = -\beta/\kappa$, resulting in the observation that $|E_{\text{pv}}|$ in MgO:LN is about 2 orders of magnitude smaller than $|E_{\text{pv}}|$ in CLN and also 2 orders of magnitude smaller than $|E_{\text{pyro}}|$ under typical conditions in these experiments. This observation reconfirms the assumption made in Subsection 3.B that $|E_{\text{pv}}| \ll |E_{\text{pyro}}|$ for MgO:LN and the parameters used in these experiments and justifies the neglect of bulk-photovoltaic effects in our analysis of the observed beam scattering in MgO:LN. Another difference between MgO:LN and CLN is the magnitude of the dielectric time constant τ_{di} , which, according to Eq. (18), is correlated to the specific photoconductivity κ . In MgO:LN E_{pyro} is screened rapidly in the illuminated parts of the crystals, $\tau_{\text{di}} = 14\text{ s}$ (Fig. 9). In contrast, in CLN screening of E_{pyro} would be much slower than in MgO:LN because of the more than 30 times smaller κ (Fig. 12). Hence, it is possible that pyroelectrically induced PRD also

occurs in CLN but could not be measured in the observation time window due to the much longer characteristic time constant.

There might also be a positive aspect of being able to change the refractive index in MgO:LN due to pyroelectrically induced PRD; e.g., it provides an efficient way to write holograms in MgO:LN with visible light because the light intensities used to create this effect are rather low. Furthermore, instead of using E_{pyro} , one might simply apply an external field E_0 , which makes the experiment more controllable. If it is also possible to fix the holograms, it would be possible to write Bragg gratings into MgO:LN crystals and use them for optical applications and combine them with the frequency conversion applications of MgO:LN.

6. CONCLUSION

It was demonstrated, theoretically and experimentally, that 5 mol.% MgO-doped LiNbO₃, which is widely known as being optical-damage resistant, can indeed suffer from PRD if a pyroelectric field is created by homogenous heating of the crystal and the crystal is illuminated with visible radiation at the same time and that this damage can be partly reversed after some time with uniform illumination with visible light. We showed that the observed beam distortion was created by a refractive index change inside the MgO:LN crystal and that a green laser beam with 1 W/cm^2 intensity, which was transmitted through the crystal in the x direction, created a maximum refractive index change of about 8×10^{-5} when the crystal was heated by 3°C . When the same experiments were performed with undoped CLN, the refractive index step was less than 10^{-6} (maximum illumination time 160 s). Furthermore, we showed that a flat-top refractive index profile was created when illumination continued because the increased photoconductivity in the illuminated area caused fast screening of E_{pyro} in the illuminated part of the crystal, whereas this was not the case in the dark parts. As soon as this refractive index change reached a flat-top profile, the beam shape slowly recovered as well. Our experiments and simulations have also proven that, with respect to pyroelectrically induced PRD, the behavior of MgO:LN is more similar to that of a medium having no bulk-photovoltaic effect, such as SBN [9], than to CLN, which has a large bulk-photovoltaic effect.

Measurements of the specific photoconductivity κ and the bulk-photovoltaic field E_{pv} confirmed that, in MgO:LN, the bulk-photovoltaic field was negligible compared to the pyroelectric fields under the conditions investigated here. Furthermore, the specific conductivity κ was found to be more than 30 times smaller and E_{pv} was up to 2 orders of magnitude larger in CLN than in MgO:LN. This difference in transport properties partly explains why the same beam distortion was not measured in CLN, because in CLN the small photoconductivity could not screen E_{pyro} in experimentally relevant time scales.

Finally, we showed theoretically that pyroelectrically induced PRD does not only occur when the temperature of the crystal is changed homogeneously, but also results from the spatially inhomogeneous thermal fields associated with beam self-heating from absorption of optical beams. This effect makes pyroelectrically induced PRD so important for non-linear optical applications using MgO:LN: if there is a strong pump laser beam that heats the crystal due to absorption and that also accidentally produces some parasitic visible

radiation, pyroelectrically induced refractive index changes can occur. And, if no volume-screening mechanism such as flood illumination with visible light is introduced to mitigate these refractive index changes, this can lead to pyroelectrically induced PRD. We also calculated that periodic poling with 50% duty cycle can reduce the pyroelectric field up to 2 orders of magnitude under typical experimental conditions.

ACKNOWLEDGMENTS

J. S. gratefully acknowledges funding provided by Deutsche Telekom Stiftung and Crystal Technology, Inc. Funding was also provided by Air Force Office of Scientific Research (AFOSR) grant FA9550-09-1-0233. We thank Boris Sturman for fruitful discussions.

REFERENCES

- R. S. Weis and T. K. Gaylord, "Lithium niobate: summary of physical properties and crystal structure," *Appl. Phys. A* **37**, 191–203 (1985).
- M. M. Fejer, G. A. Magel, D. H. Jundt, and R. L. Byer, "Quasi-phase-matched second harmonic generation—tuning and tolerances," *IEEE J. Quantum Electron.* **28**, 2631–2654 (1992).
- I. Breunig, M. Falk, B. Knabe, R. Sowade, K. Buse, P. Rabiei, and D. H. Jundt, "Second harmonic generation of 2.6 W green light with thermoelectrically oxidized undoped congruent lithium niobate crystals below 100 °C," *Appl. Phys. Lett.* **91**, 221110 (2007).
- G. D. Miller, R. G. Batchko, W. M. Tulloch, D. R. Weise, M. M. Fejer, and R. L. Byer, "42%-efficient single-pass cw second-harmonic generation in periodically poled lithium niobate," *Opt. Lett.* **22**, 1834–1836 (1997).
- D. A. Bryan, R. Gerson, and H. E. Tomaschke, "Increased optical damage resistance in lithium niobate," *Appl. Phys. Lett.* **44**, 847–849 (1984).
- D. Georgiev, V. P. Gapontsev, A. G. Dronov, M. Y. Vyatkin, A. B. Rulkov, S. V. Popov, and J. R. Taylor, "Watts-level frequency doubling of a narrow line linearly polarized Raman fiber laser to 589 nm," *Opt. Express* **13**, 6772–6776 (2005).
- H. Furuya, A. Morikawa, K. Mizuuchi, and K. Yamamoto, "High-beam-quality continuous wave 3 W green-light generation in bulk periodically poled MgO:LiNbO₃," *Jpn. J. Appl. Phys.* **45**, 6704–6707 (2006).
- Y. Furukawa, K. Kitamura, S. Takekawa, A. Miyamoto, M. Terao, and N. Suda, "Photorefractive in LiNbO₃ as a function of [Li]/[Nb] and MgO concentrations," *Appl. Phys. Lett.* **77**, 2494–2496 (2000).
- W. W. Clark, III, G. L. Wood, M. J. Miller, E. J. Sharp, G. J. Salamo, B. Monson, and R. R. Neurgaonkar, "Enhanced photorefractive beam fanning due to internal and external fields," *Appl. Opt.* **29**, 1249–1258 (1990).
- K. Buse, R. Pankrath, and E. Krätzig, "Pyroelectrically induced photorefractive damage in Sr_{0.61}Ba_{0.39}Nb₂O₆:Ce," *Opt. Lett.* **19**, 260–262 (1994).
- K. Buse and K. H. Ringhofer, "Pyroelectric drive for light-induced charge transport in the photorefractive process," *Appl. Phys. A* **57**, 161–165 (1993).
- K. Buse, "Thermal gratings and pyroelectrically produced charge redistribution in BaTiO₃ and KNbO₃," *J. Opt. Soc. Am. B* **10**, 1266–1275 (1993).
- G. T. Niitsu, H. Nagata, and A. C. M. Rodrigues, "Electrical properties along the *x* and *z* axes of LiNbO₃ wafers," *J. Appl. Phys.* **95**, 3116–3119 (2004).
- S. Sochava, K. Buse, and E. Krätzig, "Non-steady-state photocurrent technique for the characterization of photorefractive BaTiO₃," *Opt. Commun.* **98**, 265–268 (1993).
- U. Dörfler, T. Granzow, T. Woike, M. Wöhlecke, M. Imlau, and R. Pankrath, "Intensity and wavelength dependence of the photoconductivity in Cr-doped Sr_{0.61}Ba_{0.39}Nb₂O₆," *Eur. Phys. J. B* **38**, 19–24 (2004).
- L. Kanaev, V. Malinovsky, and B. Sturman, "Investigation of photoinduced scattering in LiNbO₃ crystals," *Opt. Commun.* **34**, 95–100 (1980).
- M. A. Ellabban, R. A. Rupp, and M. Fally, "Reconstruction of parasitic holograms to characterize photorefractive materials," *Appl. Phys. B* **72**, 635–640 (2001).
- M. Luennemann, U. Hartwig, and K. Buse, "Improvements of sensitivity and refractive-index changes in photorefractive iron-doped lithium niobate crystals by application of extremely large external electric fields," *J. Opt. Soc. Am. B* **20**, 1643–1648 (2003).
- A. A. Zozulya and D. Z. Anderson, "Propagation of an optical beam in a photorefractive medium in the presence of a photogalvanic nonlinearity or an externally applied electric field," *Phys. Rev. A* **51**, 1520–1532 (1995).
- M. Mitchell and M. Segev, "Self-trapping of incoherent white light," *Nature* **387**, 880–883 (1997).
- T. Bartholomäus, K. Buse, C. Deuper, and E. Krätzig, "Pyroelectric coefficients of LiNbO₃ crystals of different compositions," *Phys. Status Solidi A* **142**, K55–K57 (1994).
- F. Johann and E. Soergel, "Quantitative measurement of the surface charge density," *Appl. Phys. Lett.* **95**, 232906 (2009).
- J. Safioui, F. Devaux, and M. Chauvet, "Pyroliton: pyroelectric spatial soliton," *Opt. Express* **17**, 22209–22216 (2009).
- N. Korneeov, D. Mayorga, S. Stepanov, A. Gerwens, K. Buse, and E. Krätzig, "Enhancement of the photorefractive effect by homogeneous pyroelectric fields," *Appl. Phys. B* **66**, 393–396 (1998).
- E. Fazio, F. Renzi, R. Rinaldi, M. Bertolotti, M. Chauvet, W. Ramadan, A. Petris, and V. Vlad, "Screening-photovoltaic bright solitons in lithium niobate and associated single-mode waveguides," *Appl. Phys. Lett.* **85**, 2193–2195 (2004).
- K. Buse, "Light-induced charge transport processes in photorefractive crystals II: materials," *Appl. Phys. B* **64**, 391–407 (1997).
- S. Gronenborn, B. Sturman, M. Falk, D. Haertle, and K. Buse, "Ultraslow shock waves of electron density in LiNbO₃ crystals," *Phys. Rev. Lett.* **101**, 116601 (2008).
- M. Taya, M. C. Brashaw, and M. M. Fejer, "Photorefractive effects in periodically poled ferroelectrics," *Opt. Lett.* **21**, 857–859 (1996).
- C. M. Gómez Sarabia, P. A. Márquez Aguilar, J. J. Sánchez Mondragón, S. Stepanov, and V. Vysloukh, "Dynamics of photo-induced lens formation in a photorefractive Bi₁₂TiO₂₀ crystal under an external dc electric field," *J. Opt. Soc. Am. B* **13**, 2767–2774 (1996).
- M. C. Wengler, U. Heinemeyer, E. Soergel, and K. Buse, "Ultra-violet light-assisted domain inversion in magnesium-doped lithium niobate crystals," *J. Appl. Phys.* **98**, 064104 (2005).
- W. Huafu, S. Guotong, and W. Zhongkang, "Photovoltaic effect in LiNbO₃:Mg," *Phys. Status Solidi A* **89**, K211–K213 (1985).
- M. Koesters, B. Sturman, D. Haertle, and K. Buse, "Kinetics of photorefractive recording for circular light beams," *Opt. Lett.* **34**, 1036–1038 (2009).
- D. Kip, E. Krätzig, V. Shandarov, and P. Moretti, "Thermally induced self-focusing and optical beam interactions in planar strontium barium niobate waveguides," *Opt. Lett.* **23**, 343–345 (1998).
- J. S. Pelc, C. Langrock, Q. Zhang, and M. M. Fejer, "Influence of domain disorder on parametric noise in quasi-phase-matched quantum frequency converters," *Opt. Lett.* **35**, 2804–2806 (2010).
- K. K. Wong, *Properties of Lithium Niobate* (INSPEC, 2002).
- J. P. Gordon, R. C. C. Leite, R. S. Moore, S. P. S. Porto, and J. R. Whinnery, "Long-transient effects in lasers with inserted liquid samples," *J. Appl. Phys.* **36**, 3–8 (1965).
- M. Koesters, C. Becher, D. Haertle, B. Sturman, and K. Buse, "Charge transport properties of undoped congruent lithium niobate crystals," *Appl. Phys. B* **97**, 811–815 (2009).
- W. Koehler, *Solid-State Laser Engineering* (Springer, 1999).
- B. Cole, L. Goldberg, V. King, and L. Leach, "Influence of UV illumination on the cold temperature operation of a LiNbO₃ Q-switched Nd:YAG laser," *Opt. Express* **18**, 9622–9627 (2010).
- D. S. Hum, R. K. Route, G. D. Miller, V. Kondilenko, A. Alexandrovski, J. Huang, K. Urbanek, R. L. Byer, and M. M. Fejer, "Optical properties and ferroelectric engineering of vapor-transport-equilibrated, near-stoichiometric lithium tantalate for frequency conversion," *J. Appl. Phys.* **101**, 093108 (2007).